Electronic Supplementary Information

A nuclei-rich strategy for highly reversible dendrite-free zinc metal anodes

Qingli Zou, Zhuojian Liang, Wanwan Wang, Dejian Dong & Yi-Chun Lu*

Electrochemical Energy and Interfaces Laboratory, Department of Mechanical and Automation Engineering, The Chinese University of Hong Kong, Hong Kong, SAR 999077, China.

* E-mail: yichunlu@mae.cuhk.edu.hk

Content

1. Experiment section

Preparation of nuclei-rich electrodes

The Zn foil was polished with sandpaper to remove the oxidation layer before any other operation. 0.04 g polyvinylidene fluoride (PVDF, Arkema) was first dissolved in 2 ml 1-Methyl-2-pyrrolidinone (NMP, anhydrous, 99.5%, Sigma-Aldrich) solvent at room temperature. The 0.54 g nano-hydroxyapatite (Macklin) was added to the PVDF solution and stirred for 24h to obtain coating slurry. The slurry was coated on the Zn or Cu foil and dried at 55 ℃ under vacuum overnight. The obtained electrodes were punched into circular disks with a diameter of 12mm.

Synthesis of α-MnO_2

α-MnO_2 was synthesized with a typical hydrothermal method with $MnSO_4 \cdot H_2O$ (99%, Meryer) as the source of Mn and $KMnO_4$ (≥99.0%, Honeywell Fluka) as oxidation agent. According to the literature[1], 0.003 M $MnSO_4 \cdot H_2O$ and 2 ml 0.5 M H_2SO_4 were added to 90 ml deionized water. The solution was magnetically stirred for half hour to obtain a clear solution. Then, 20 ml 0.1 M $KMnO_4$ aqueous solution was added into the obtained solution very slowly and strung for 3 h under room temperature. The solution was subsequently transferred into a hydrothermal reactor and heated at 120 °C for 12 h. The product obtained was centrifuged and washed three times with deionized water. It was then dried with a vacuum oven at room temperature to obtain α-MnO_2 powder.

Cell assembly

All the cell cases were coved with Cu tape to eliminate the water splitting.

The symmetric cells were assembled with Φ12 mm conventional Zn or nuclei-rich electrodes and Φ16 mm quartz fiber filters (QM-A, Whatman) as separators. 2 M $ZnSO_4 \cdot 7H_2O$ (99%, Macklin) was dissolved in the deionized water and applied as electrolyte.

Zn|Cu cells were assembled with the same methods with Cu as cathode current collectors.

The three-electrode cell for the CV test was assembled with an extra Ag/AgCl reference electrode. The structure of the three-electrode cell was the same as reported[2].

For the Zn-MnO_2 full cells, the cathodes were prepared with the synthesized α-MnO_2. The cathode slurry containing α-MnO_2, Ketjen Black EC-600JD (KB), and PVDF binder at a mass ratio of 7:2:1 in NMP was coated on Φ12 mm Ti meshes and dried with a vacuum oven at 60 °C. The same slurry was coated on square Ti meshes (4 cm * 5 cm) to obtain the electrodes for pouch cells. Conventional or nuclei-rich Zn electrodes were applied as anodes. Quartz fiber

filters were used as separators and 2 M $ZnSO_4$ with 0.2 M $MnSO_4$ aqueous solution was used as the electrolyte.

Electrochemical measurement

Galvanostatic charge/discharge cycling tests were carried out on a LAND 2001 CT battery tester at room temperature. Chronoamperometry (CA), Linear sweep voltammetry (LSV), Cyclic voltammetry (CV), and electrochemical impedance spectroscopy (EIS) were conducted using Bio-Logic VMP3. The data were processed with the following methods for further investigation.

Nucleation model: Current transient curve was measured by chronoamperometric technique with three electrode cells with a Zn metal reference. Cu-based conventional and nuclei-rich electrodes were applied as working electrodes to avoid the influence of the direct growth current of the original Zn crystal on the total current. 1 M Na_2SO_4 and 0.1 M $ZnSO_4$ aqueous electrolytes were applied as electrolytes. Na_2SO_4 was introduced to balance concentration polarization during Zn plating. The experiment was carried out by stepping the potential from open circuit potential to different potentials. The original curves were reported to determine the maximum point and further plot $(I/I_m)^2$ to t/t_m dimensionless curves, where I_m and t_m are the maximum current density and its corresponding time. The dimensionless curves were fitted with theoretical instantaneous (gray solid line) and progressive nucleation (gray dashed line) curves described by the Scharifker-Hills' models[3] described in Equations 1 and 2. The Zn^{2+} diffusion coefficiency (D_i or D_p), nuclei density (N), nucleation rate (AN_∞), and radius (r) were calculated with the following equations respectively, where A is the steady state nucleation rate constant per site, N_∞ is the number density of the active site.

For the instantaneous nucleation mode, N and D_i are described by Equations 3 and 5. For the progressive nucleation mode, AN_∞ and D_p can be determined from Equations 6 and 8. Here, M is the molar weight of the deposit (g mol^{-1}), ρ is the density of the deposit (g cm^{-3}), c is the concentration (mol cm^{-3}) of the electroactive species, D is the diffusion coefficient ($cm^2\ s^{-1}$) of the electroactive species, z is the number of electrons involved in the redox process, and F is the Faraday constant. The constants k and k' are defined as equations 4 and 7.

$$N = \frac{I_m^2}{0.41 z^2 F^2 D_i^2 c^2 k_i} \quad (3)$$

$$k_i = \left(\frac{8\pi c M}{\rho}\right)^{1/2} \quad (4)$$

$$D_i = \frac{I_m^2 t_m}{0.1629 (zFc)^2} \quad (5)$$

$$AN_{\infty} = \frac{I_m^4}{0.045z^4F^4D_p^3c^4k_p} \quad (6)$$

$$k_p = \frac{4}{3}\left(\frac{8\pi cM}{\rho}\right)^{1/2} \quad (7)$$

$$D_p = \frac{I_m^2 t_m}{0.2598(zFc)^2} \quad (8)$$

The radius (r) of nuclei can be calculated with Equation 9. Here, Ns is the saturation nuclear density. For the instantaneous nucleation mode, N_s equals N_0, and for progressive nucleation, it could be obtained by Equation 10.[4]

$$r = \left(\frac{1}{\pi N_s}\right)^{1/2} \quad (9)$$

$$N_s = \left(\frac{AN_{\infty}}{2k_pD_p}\right)^{1/2} \quad (10)$$

Tafel plots: The original LSV data was processed to obtain the Tafel plots. The cathodic and anodic Tafel regions were linear fitted and the exchange current was obtained from the intersection of the fitting lines.

Arrhenius plots: The temperature (T) dependent EIS data were collected. The charge transfer resistances (R_{ct}) were obtained by fitting the original data with the equivalent circuit. The data were plotted with $\ln(1/R_{ct})$ versus 1/T and linear fitted to obtain Arrhenius plots. The activation energy (E_a) was calculated with the slope of the fitted line, according to the Arrhenius Equation (Equation 11)[5]. Here, R is the universal gas constant and A is a non-thermal constant.

$$\ln\left(\frac{1}{R_{ct}}\right) = \left(-\frac{E_a}{R}\right)\left(\frac{1}{T}\right) + lnA \quad (11)$$

Cumulative capacity: Cumulative capacity is calculated by multiplying current density by the total time of Zn plating based on the symmetric cell cycling result.[6] The comparison data was calculated according to the same method as the cycling results collected from the literature.

Material and Electrode Characterization

The electrode collected after a certain operation was washed three times with deionized water and dried under vacuum at room temperature before characterization. SEM was performed

using a JSM7800F (JEOL, Japan). XRD was conducted with a Rigaku Smartlab diffractometer (Cu Kα radiation).

OEMS measurements

OEMS tests were conducted as reported[7, 8]. Ar carrier gas continuously transferred the gas evolved in the cell to a mass spectrometer (QMS 200, Stanford Research Systems) for analysis. The quantification of gas was calibrated using a standard gas mixture of O_2, CO_2, CO, H_2, and H_2O (5000 ppm each, rest balanced by Ar).

DFT calculations

The DFT calculations were carried out using the Vienna Ab-initio Simulation Package (VASP)[9, 10] with the frozen-core all-electron projector-augment-wave (PAW)[11, 12] methods. The Perdew-Burke-Ernzerhof (PBE)[13] of generalized gradient approximation (GGA) was adopted to describe the exchange and correlation potential. The cutoff energy for the plane-wave basis set was set to 450 eV. The 2-layer hydroxyapatite slabs were used, and a vacuum region of 15 Å above them was used to ensure the decoupling between neighboring systems. For the zinc surface, A 5-layer 4×4 Zn slab was used. The geometry optimizations were performed until the forces on each ion were reduced below 0.01 eV/Å. The 3×3×1 k-point[14] sampling of the Brillouin zone was used. The DFT-D3 method was used to describe the van der Waals interaction[15].

The adsorption energy, E_{ads}, is calculated with Equation (12).

$$E_{ads} = E_{Zn+surface} - E_{surface} - E_{Zn} \quad (12)$$

where $E_{surface}$ is the energy of the hydroxyapatite and Zn slabs, E_{Zn} represents the energy of the Zn, and $E_{Zn+surface}$ represents the total energy of the adsorbed system.

2. Supplementary figures

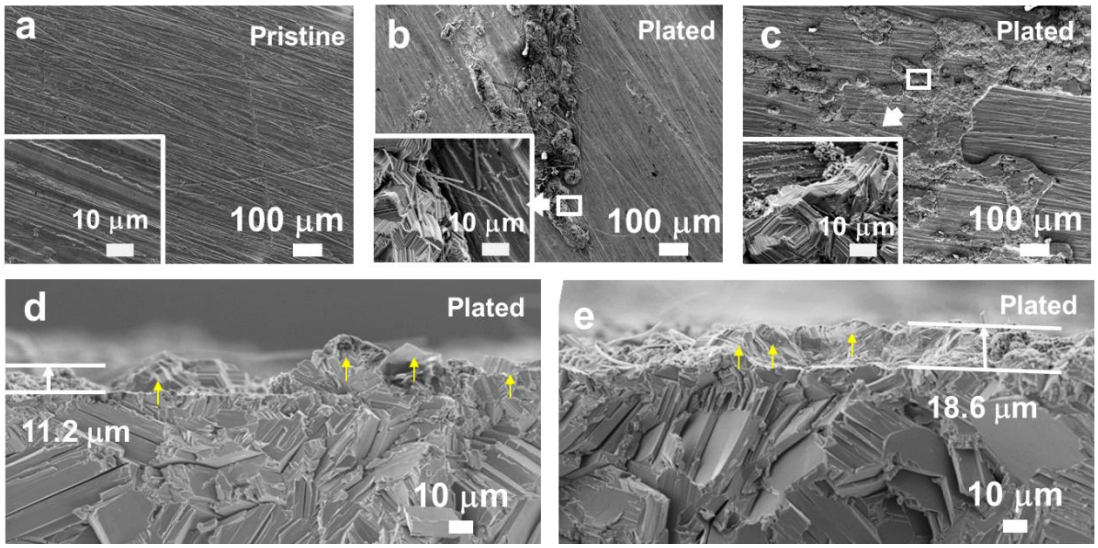

Fig. S1 Morphology of conventional Zn electrodes after plating. (a) Pristine Zn electrode. (b, c) Top-view and (d, e) sectional-view SEM images of the conventional electrode after plating with a current density of (b, d) 1 mA cm^{-2} and (c, e) 5 mA cm^{-2} for 40 min.

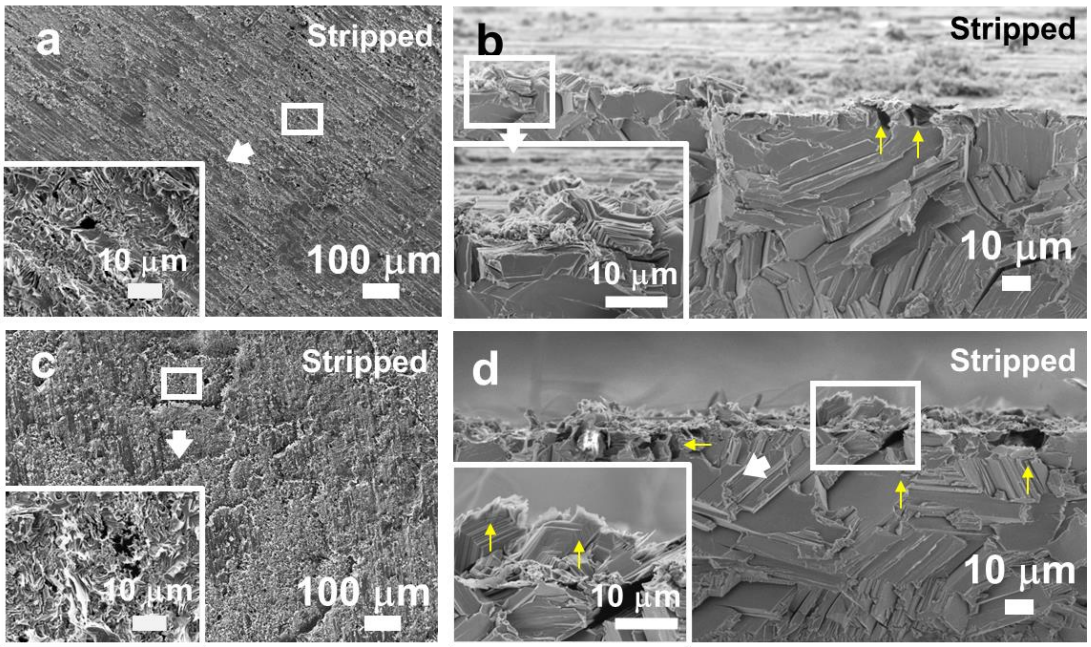

Fig. S2 Morphology of conventional Zn electrodes after stripping. (a, c) Top-view and (b, d) sectional-view SEM images of the conventional electrode after stripping with a current density of (a, b) 1 mA cm^{-2} and (c, d) 5 mA cm^{-2} for 40 min.

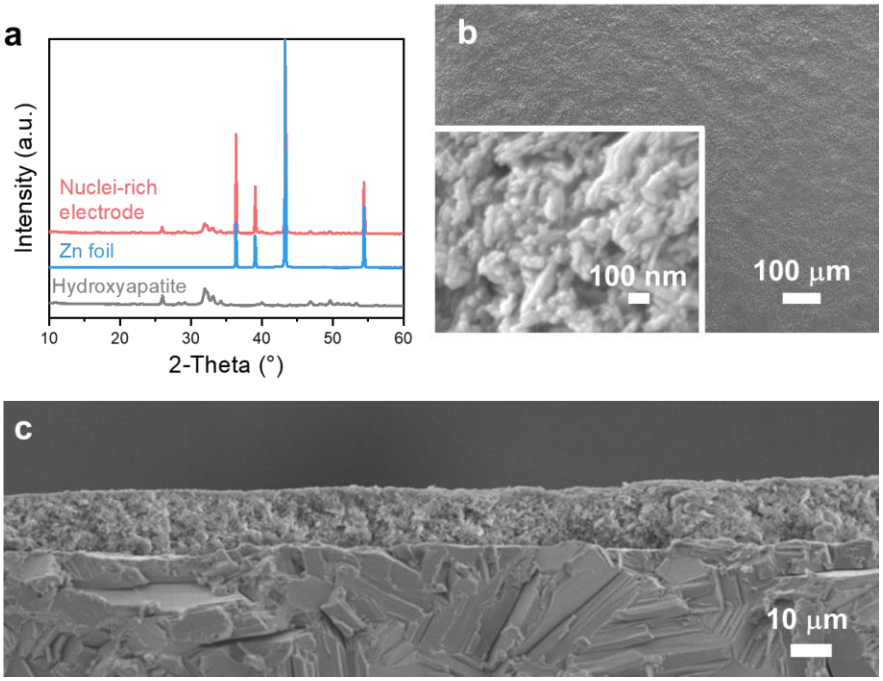

Fig. S3 Characterization of the nuclei-rich electrode. (a) Comparison of XRD profiles of the nuclei-rich electrode to Zn foil and hydroxyapatite. (b) Top-view and (c) sectional-view SEM image of the nuclei-rich electrode.

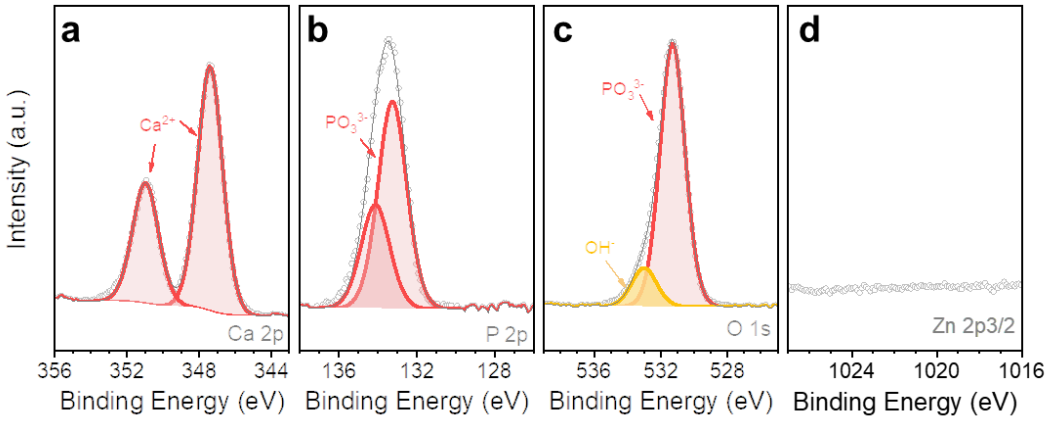

“

Fig S4 The XPS spectra of (a) Ca 2p, (b) P 2p, (c) O 1s, and (d) Zn $2p_{3/2}$ of the nuclei-rich electrode.

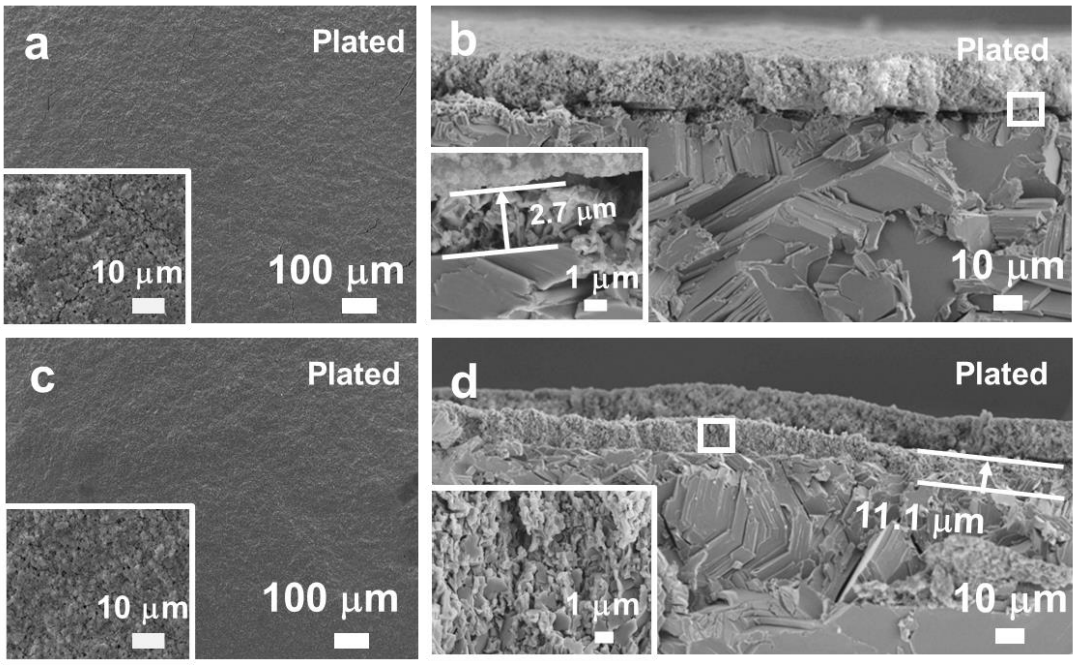

Fig. S5 Morphology of nuclei-rich electrodes after plating. (a, c) Top-view and (b, d) sectional-view SEM images of the nuclei-rich electrode after plating with a current density of (a, b) 1 mA cm^{-2} and (c, d) 5 mA cm^{-2} for 40 min.

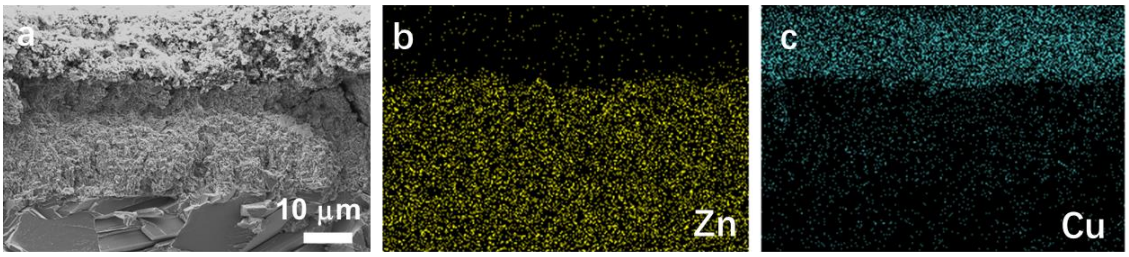

Fig. S6 (a) The sectional-view SEM image of nuclei-rich Zn electrode after plating with a current density of 15 mA cm^{-2} for 40 min. (b-c) The EDS mapping image of (a)

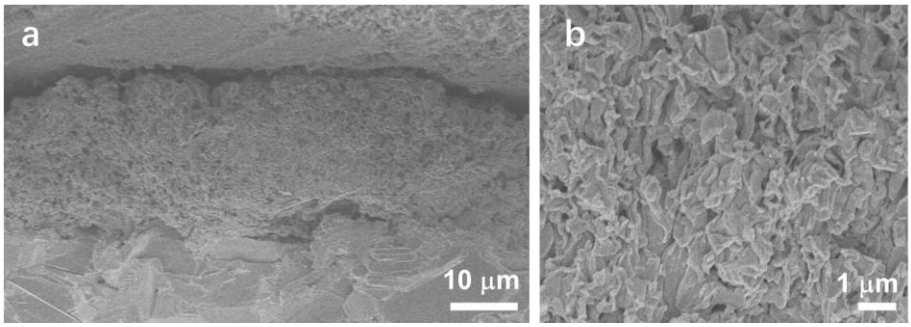

Fig. S7 (a) The sectional-view SEM image of nuclei-rich Zn electrode after stripping first and then plating at current density of 5 mA cm^{-2} for 40 min, (b) The zoom in image of (a)."

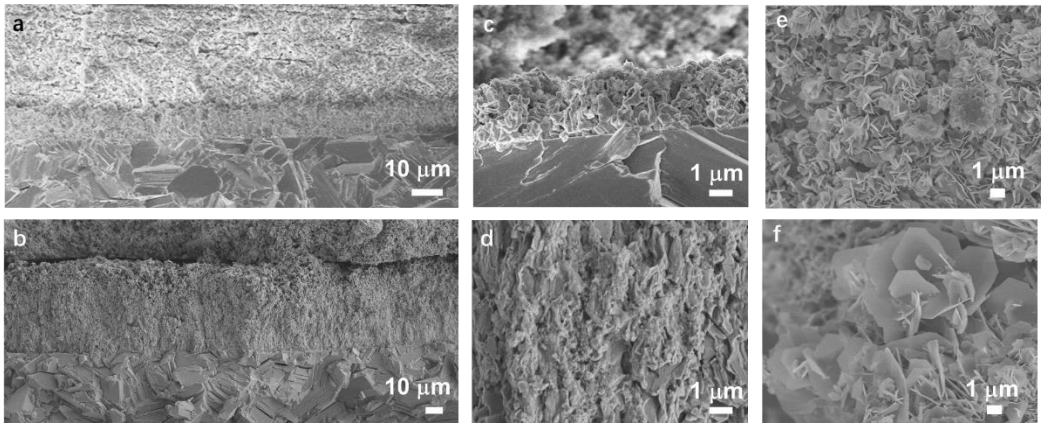

Fig. S8 Cross-sectional SEM image of nuclei-rich electrode after plating at 5 mA cm^{-2} for (a) 20 min, and (b)120 min. (c) and (d) is the high magnification SEM image focusing on the plating layer of (a) and (b). Top-view SEM image of conventional electrode after plating at 5 mA cm^{-2} for (e) 20 min, and (f)120 min.

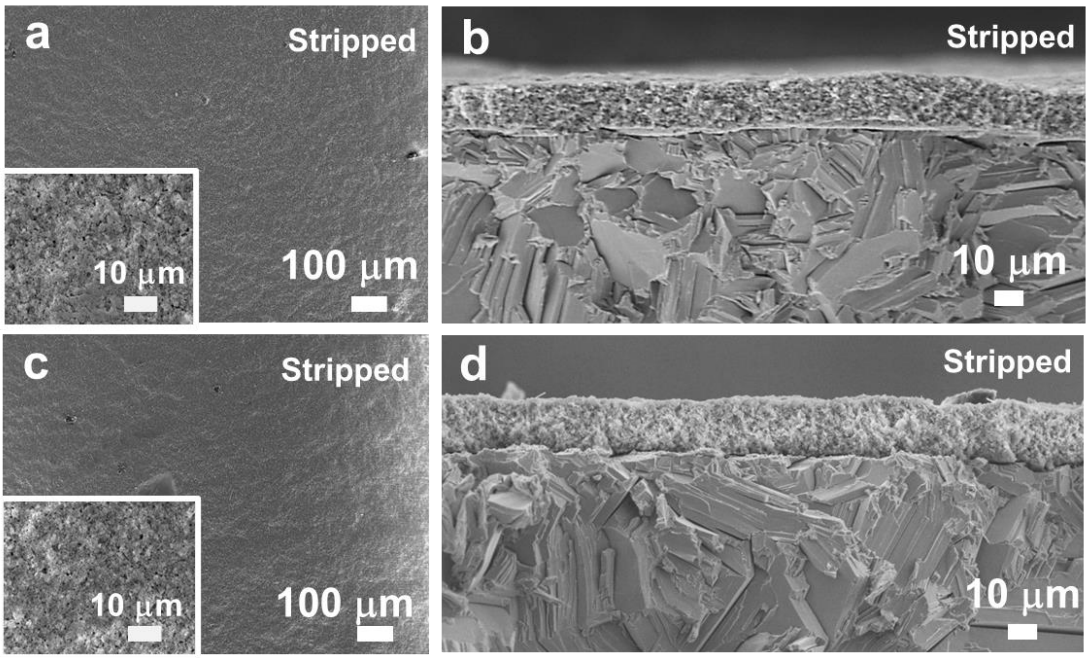

Fig. S9 Morphology of nuclei-rich electrodes after plating and stripping. (a, c) Top-view and (b, d) sectional-view SEM images of the nuclei-rich electrode after stripping with a current density of (a, b) 1 mA cm^{-2} and (c, d) 5 mA cm^{-2} for 40 min.

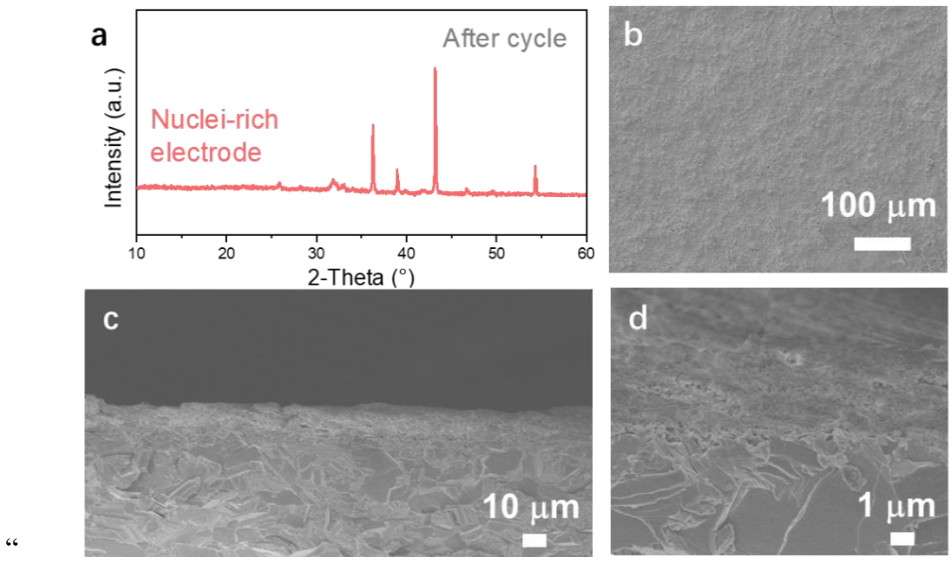

“

Fig. S10 (a) XRD profiles, (b) top-view, and (c-d) sectional-view SEM images of the nuclei-rich electrode after 30 plating and stripping cycles at 1 mA cm^{-2} and 1 mAh cm^{-2}.

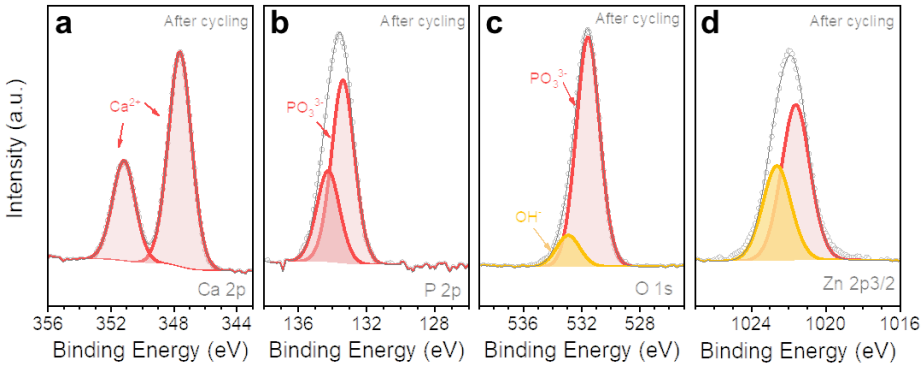

Fig S11 The XPS spectra of (a) Ca 2p, (b) P 2p, (c) O 1s, and (d) Zn $2p_{3/2}$ of the nuclei-rich electrode after 30 plating and stripping cycles at 1 mA cm^{-2} and 1 mAh cm^{-2}.

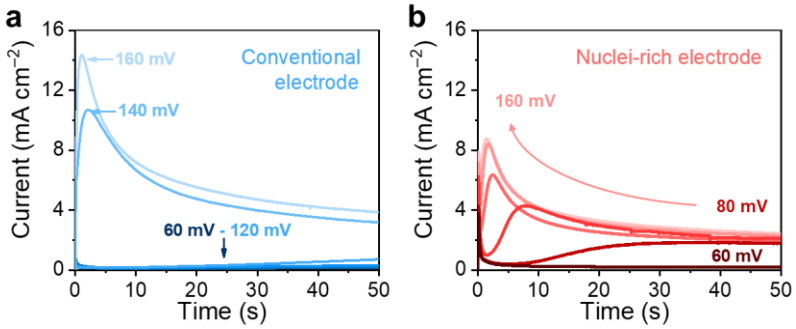

Fig. S12 Chronoamperometric test. The current transient curves of (a) conventional and (b) nuclei-rich electrodes with different overpotentials of 60 mV, 80 mV, 100 mV, 120 mV, 140 mV, and 160 mV. The color of the lines from dark to light represents the increase of overpotential.

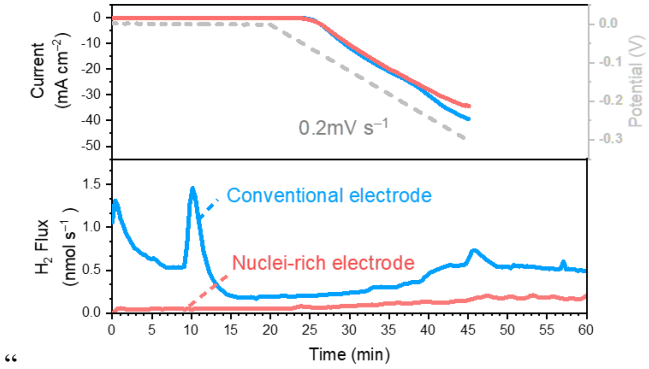

Fig. S13 Inhibited H_2 evolution. H_2 evolution from LSV scanning symmetric cells with conventional and nuclei-rich electrodes

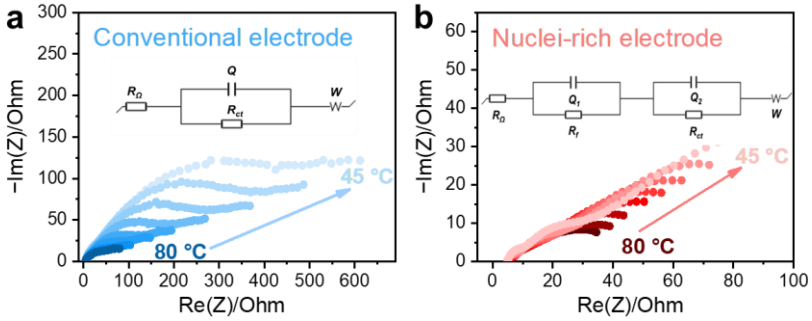

Fig. S14 Temperature-dependent resistance for Arrhenius plots. Electrochemical impedance spectroscopy data that collected with (a) conventional and (b) nuclei-rich Zn electrodes with temperature controlled from 45 to 80 °C with a common difference of 5 °C. The equivalent circuits applied for fitting are inserted.

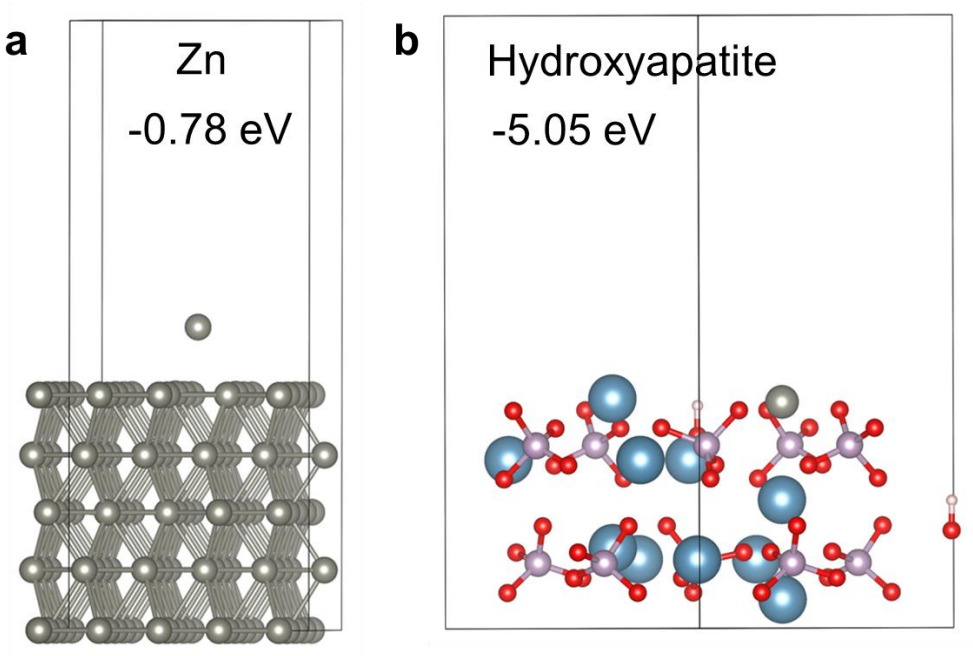

Fig. S15 Enhanced Zn adsorption. Computational models of Zn atoms adsorbed on the surface of (a) Zn metal and (b) hydroxyapatite.

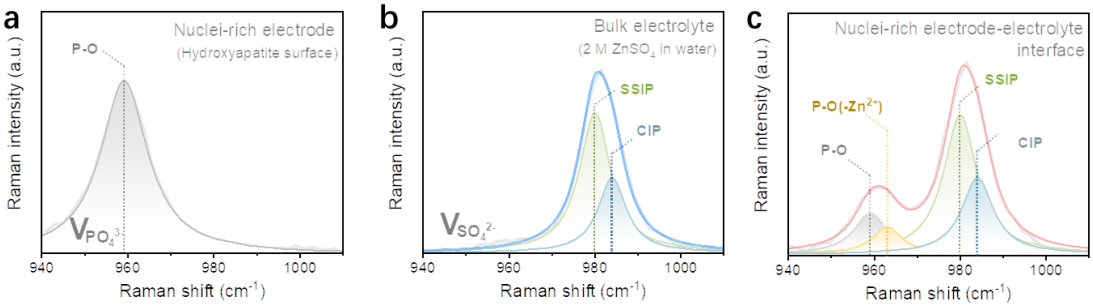

Fig. S16 Raman spectra of (a) nuclei-rich electrode, (b) bulk electrolyte, and (c) nuclei-rich electrode-electrolyte interface. Two presentative solvation structure of Zn^{2+} are denoted as SSIP(hexahydrate or solvation separated ion pairs, $[Zn^{2+}(H_2O)_6{\cdot}SO_4^{2-}]$) and CIP (contact ion pairs, $[Zn^{2+}(H_2O)_5{\cdot}OSO_3^{2-}]$).

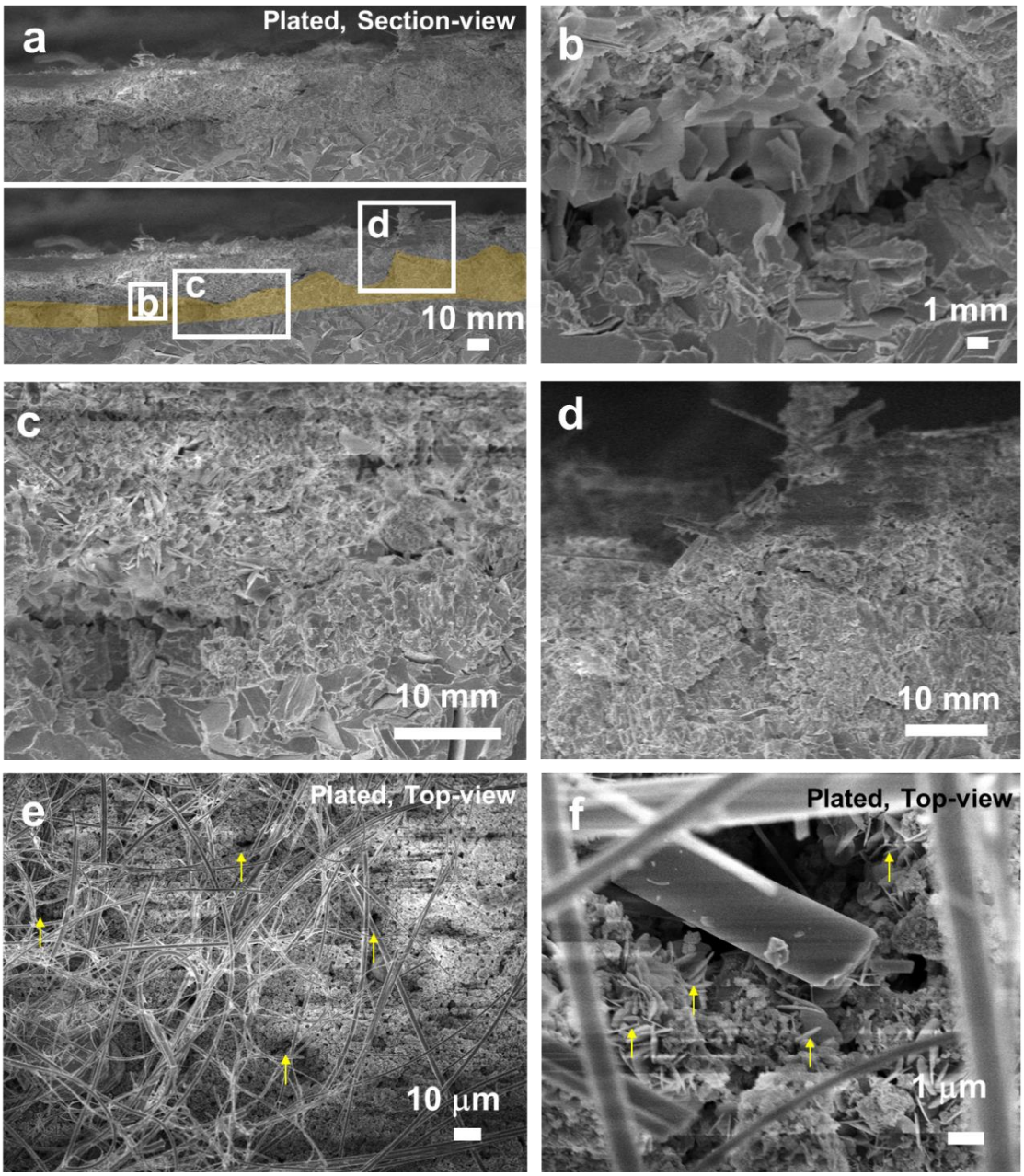

Fig. S17 Morphology of ZCB electrodes after plating. (a-d) The sectional-view and (e, f) top-view SEM images of ZCB electrodes after plating with a current density of 15 mA cm^{-2} and areal capacity of 10 mAh cm^{-2}. The top half of (a) is the original SEM image and the bottom half is the processed image with plated Zn highlighted in yellow and the location of magnified images (b-d) marked. The yellow arrows point out the holes (c) and Zn tablets (d).

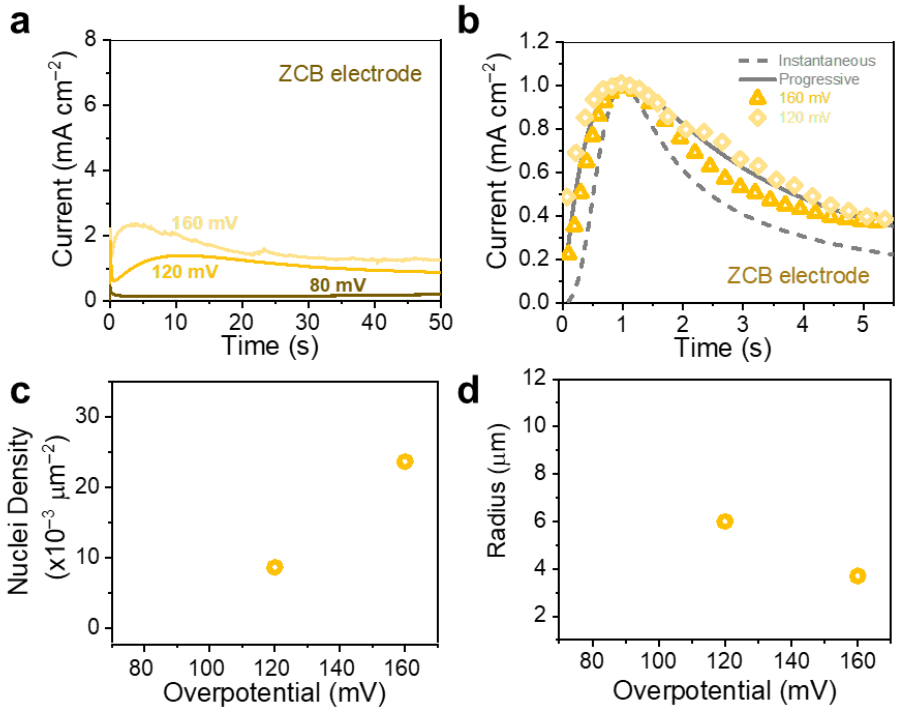

Fig. S18 Nucleation mode of Zn plating and stripping on ZCB electrode. (a) The current transient curves of ZCB electrode with different overpotentials of 60 mV, 80 mV, 100 mV, 120 mV, 140 mV, and 160 mV. The color of the lines from dark to light represents the increase of overpotential. (b) Dimensionless curves of Zn plating on ZCB electrodes with theoretical instantaneous (gray dashed line) and progressive nucleation (gray solid line) curves described by the Scharifker-Hills' models. (c) nuclei density and (d) radius of Zn plating on ZCB electrodes at various overpotentials.

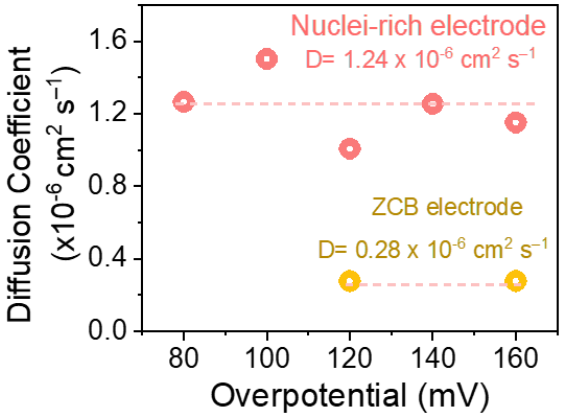

Fig. S19 Comparison of Zn^{2+} conducting ability. The diffusion coefficient of Zn^{2+} that measured with the nuclei-rich electrode and ZCB electrode.

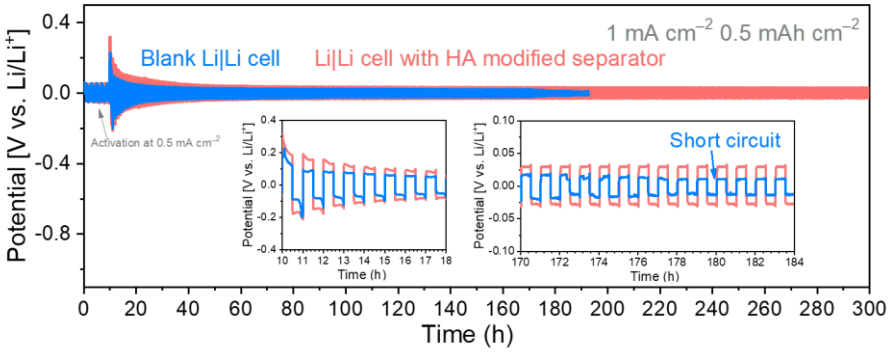

Fig. S20 Cycling profiles of Li symmetric cells with current density and areal capacity of 1 mA cm^{-2} and 0.5 mAh cm^{-2}.

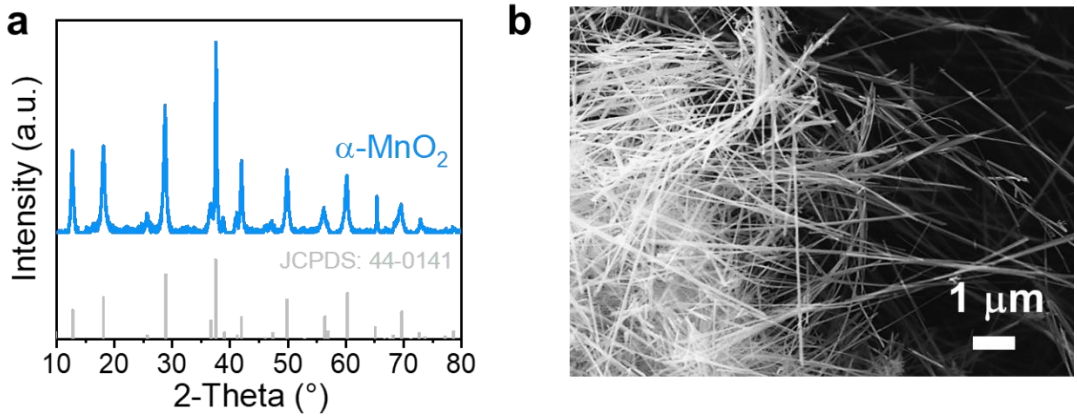

Fig. S21 Characterization of synthesized α-MnO_2. (a) XRD profile and (b) SEM image of synthesized α-MnO_2.

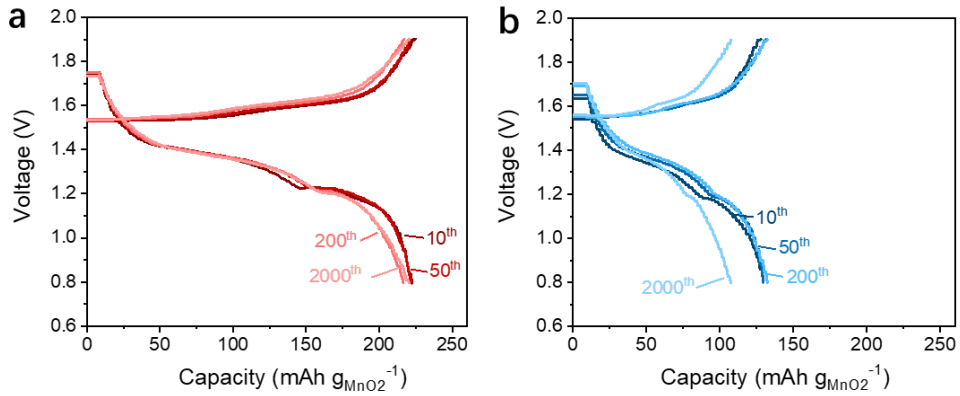

Fig. S22 Voltage profile of Zn-MnO_2 full cell at various cycle numbers.

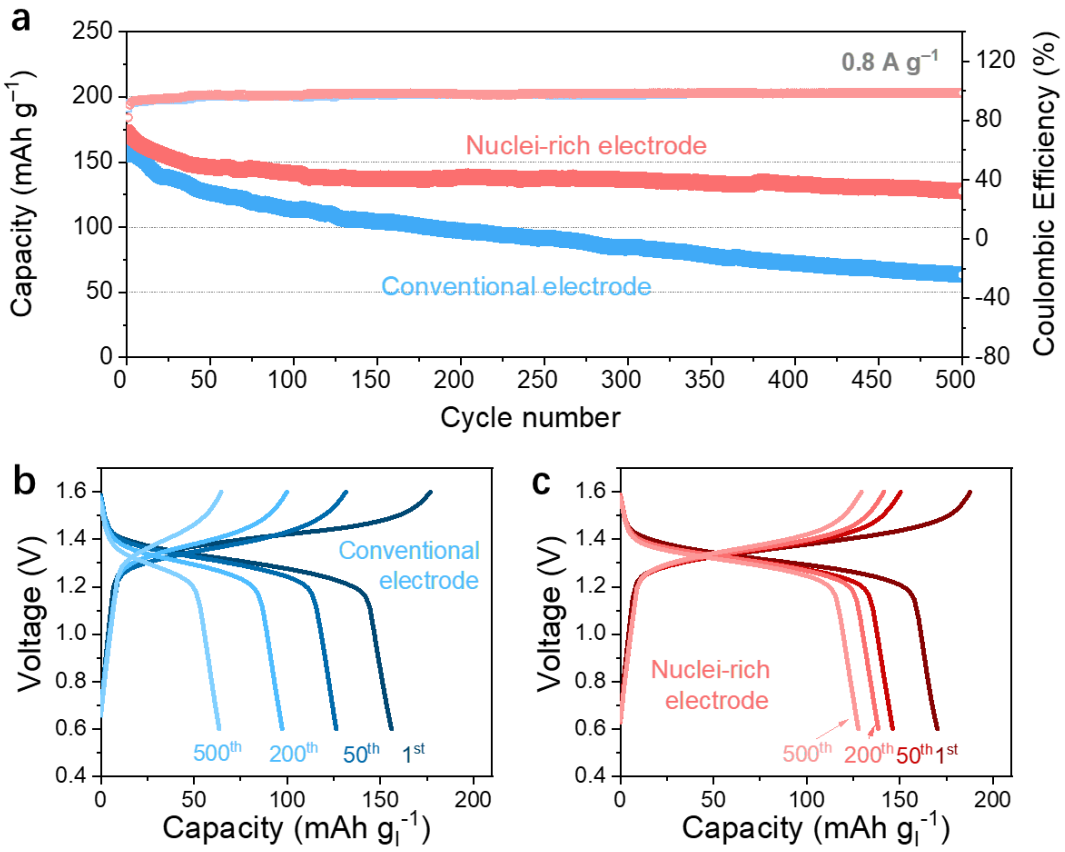

Fig. S23 (a) Cycling profile of Zn-I_2 full cells with conventional and nuclei-rich Zn electrodes. Voltage profile of Zn-I_2 full cell with (b) conventional and (c) nuclei-rich Zn electrodes.

Table S1 Comparison of electrochemical performances of various cathode materials for aqueous zinc-ion batteries.

Cathode material	Initial discharge capacity (mA h g^{-1})	Current density (mA g^{-1})	Reference
α-MnO_2	**228**	**3000**	**This work**
MnO_2/MoO_3	333	100	ACS nano, 2023,17, 14792
β-MnO_2	270	100	J. Mater. Chem. A, 2017, 5 , 23299

Mn_2O_3	78	100	Electrochim. Acta, 2018, 259 , 170
Mn_3O_4	232	200	J. Mater. Chem. A, 2018, 6 , 9677
CoHCF	187.3	250	Adv. Mater.2020,32, 1908121
CuHCF	70.4	300	ACS Appl. Energy Mater.2019,2, 6984
VO_2(M)	248	2000	J. Mater. Chem. A, 2020, 8, 1731
rGO/VO_2	276	100	Energy Storage Mater., 2019, 17 , 143
Amorphous V_2O_5/graphene	489	100	Adv. Energy Mater., 2020, 10, 2000081
$V_2O_5{\cdot}nH_2O$ (GAVOH)	215	2000	Adv. Funct. Mater.2023, 33, 2211412
carbon-coated V_2O_5 microspheres	532.4	200	ACS Sustainable Chem. Eng. 2023, 11, 13298
$Li_xV_2O_5{\cdot}nH_2O$	407.6	1000	Energy Environ. Sci., 2018, 11 , 3157
$H_2V_3O_8$/graphene	394	100	Adv. Energy Mater., 2018, 8 , 1800144
$V_6O_{13}{\cdot}nH_2O$	395	100	ACS Appl. Energy Mater., 2019, 2 , 1988
$Zn_2V_2O_7$	248	50	J. Mater. Chem. A, 2018, 6 , 3850
$NaV_3O_8{\cdot}1.5H_2O$	380	50	Nat. Commun., 2018, 9 , 1656
MoS_2	232	100	Nano Lett.2019,19, 3199
MoS_2	202.6	100	Energy Storage Mater.2019,19, 94

3. Reference

1. H. Pan, Y. Shao, P. Yan, Y. Cheng, K. S. Han, Z. Nie, C. Wang, J. Yang, X. Li and P. Bhattacharya, *Nat. Energy*, 2016, **1**, 1-7.
2. Q. Zou, Y. Sun, Z. Liang, W. Wang and Y. C. Lu, *Adv. Energy Mater.*, 2021, 11, 2101552.
3. B. Scharifker and G. Hills, *Electrochim. Acta*, 1983, **28**, 879-889.
4. L. Legrand, A. Tranchant and R. Messina, *J. Electrochem. Soc.*, 1994, **141**, 378.
5. K. J. Laidler, *Journal of chemical Education*, 1984, **61**, 494.
6. L. Ma, M. A. Schroeder, O. Borodin, T. P. Pollard, M. S. Ding, C. Wang and K. Xu, *Nat. Energy*, 2020, **5**, 743-749.
7. Z. Liang, Q. Zou, J. Xie and Y.-C. Lu, *Energy Environ. Sci.*, 2020, **13**, 2870-2877.
8. Z. Liang and Y.-C. Lu, *J. Am. Chem. Soc.*, 2016, **138**, 7574-7583.
9. G. Kresse and J. Furthmüller, *Physical review B*, 1996, **54**, 11169.
10. G. Kresse and J. Hafner, *Physical Review B*, 1994, **49**, 14251.
11. P. E. Blöchl, *Physical review B*, 1994, **50**, 17953.
12. G. Kresse and D. Joubert, *Physical review b*, 1999, **59**, 1758.
13. B. Hammer, L. B. Hansen and J. K. Nørskov, *Physical review B*, 1999, **59**, 7413.
14. H. J. Monkhorst and J. D. Pack, *Physical review B*, 1976, **13**, 5188.
15. S. Grimme, J. Antony, S. Ehrlich and H. Krieg, *J. Chem. Phys.*, 2010, **132**, 154104.